



Suppressing the aromatic cycle of the dimethyl ether to hydrocarbons reaction on zeolites

Benjamin Niethammer, Ulrich Arnold^{*}, Jörg Sauer

Institute of Catalysis Research and Technology (IKFT), Karlsruhe Institute of Technology (KIT), Hermann-von-Helmholtz-Platz 1, 76344 Eggenstein-Leopoldshafen, Germany

ARTICLE INFO

Keywords:

Dimethyl ether to Hydrocarbons
*MRE
Zeolites
Olefin cycle
Aromatic cycle

ABSTRACT

The influence of the zeolite framework type on the conversion of dimethyl ether (DME) to hydrocarbons (DTH) was investigated for *MRE, MFI and TON zeolite catalysts. Remarkable differences in the catalytic performance of the materials were observed. In particular, the *MRE zeolite showed an exceptionally high yield of olefins (90%) with a substantial ratio of products in the chain length range C₅-C₁₁. Additionally, the longevity of the *MRE zeolite clearly exceeded previously reported data. The comparison of mechanistic parameters (Hydrogen-Transfer-Index HTI_{CI} and C₃/C₂ ratio) demonstrated for this zeolite, that the formation of aromatics in the reaction network can be almost completely suppressed under suitable reaction conditions. By varying the reaction parameters temperature, DME partial pressure and weight hourly space velocity (WHSV), it was possible to identify the optimal combination of selectivity and deactivation resistance for each material. The olefin-rich DTH product of the *MRE zeolite offers manifold possibilities for further conversion to valuable renewably produced low-emission fuels like gasoline or jet fuel.

1. Introduction

The use of non-fossil carbon sources for fuel synthesis enables the reduction of CO₂ emissions in the transport sector. The production of hydrocarbons from regenerative carbon sources via biomass to liquid (BTL) or power to liquid (PTL) processes offers promising opportunities on the way to CO₂ neutrality in the transport sector. The conversion of dimethyl ether (DME) to hydrocarbons (DTH) could be one step in such a process chain, complementary to the well-known methanol to hydrocarbons (MTH) reaction [1–3]. Using DME as feedstock is beneficial because: (I) Single-step DME synthesis enables the utilization of syngas with lower H₂/CO ratio as well as CO₂-rich syngas in a thermodynamically more advantageous way compared to methanol synthesis [4–6]. (II) It offers an advantageous hydrocarbon production route with lower adiabatic temperature rise due to lower heat duty and (III) A higher methylation activity, reactivity, hydrocarbon product selectivity and conversion capacity can be implemented [7–11].

Starting from methanol or DME, light olefins are formed as primary hydrocarbon products, which are subsequently transformed to a mixture of paraffins, olefins and aromatics via secondary reactions in a so-called dual cycle mechanism comprising an olefin and an aromatic cycle [12].

The formation of a hydrocarbon pool (HCP) inside the catalyst bed promotes hydrocarbon production in an autocatalytic manner [13,14]. Reactant conversion and product composition of the MTH/DTH reaction highly depend on the catalyst and the process conditions. Typically, zeolites with the MFI framework type are used in MTH/DTH processes [1–3]. A matter of particular interest is the process modification to minimize the yield of aromatics and maximize the yield of olefins. Olefins with a chain length of 5 or more C-atoms (C₅₊) offer a wide range of possibilities for further processing. For example, low-emission gasoline could be produced by hydrogenation, or synthetic jet fuel could be generated by dimerization. A promising way to generate an enhanced olefin yield would be the elimination of the aromatic cycle during the product formation by selecting a zeolite catalyst with suitable shape selectivity. Efforts in this direction were made using TON framework type zeolites with unidirectional medium (10-ring) pore systems [15–17]. However, since the aromatic cycle is not completely suppressed, the aromatic products remain mainly in the narrow zeolite pores due to spatial confinement. Thus, a high olefin content prevails in the reactor effluent, but the lifetime of the catalyst is very short due to rapid deactivation [15–17]. The preparation of mesoporous nanoscale zeolite crystals was reported to counteract this rapid deactivation and

^{*} Corresponding author.

E-mail address: ulrich.arnold@kit.edu (U. Arnold).

<https://doi.org/10.1016/j.apcata.2023.119021>

Received 30 September 2022; Received in revised form 12 December 2022; Accepted 2 January 2023

Available online 3 January 2023

0926-860X/© 2023 The Authors. Published by Elsevier B.V. This is an open access article under the CC BY license (<http://creativecommons.org/licenses/by/4.0/>).

increase the longevity of the catalysts to a certain extent [18–20]. *MRE zeolites exhibit slightly larger one-dimensional 10-ring tubular pores (Table 1). These high-silica zeolites tend to form a highly complex disordered framework. The degree of disorder is variable and it does not block the pores [21]. *MRE zeolites were reported to exhibit a high C₂-C₄ selectivity, employing a high contact time and a reaction temperature below 673 K [22]. Catalyst deactivation occurred vastly faster than by using a MFI zeolite under the same conditions. A noticeable yield of paraffins in conjunction with a low yield of aromatics indicated a high deposition of unsaturated compounds on the catalyst, leading to fast coking [22]. Teketel et al. [15,23] reported a similar longevity of TON and *MRE zeolites in MTH conversion, with a significant higher selectivity to aromatics for *MRE. By investigating the MTH reaction on a *MRE zeolite in the temperature range of 723–973 K, Zhang et al. [24] achieved a high selectivity to C₃-C₆ olefins with an *MRE catalyst at comparatively low reaction temperature (723 K), while complete conversion of reactants was only maintained up to a time-on-stream (TOS) of 2.5 h, followed by a decrease of conversion below 20% in a total of less than 10 h TOS.

Within this work, compared to previous reports, deviating results of the catalytic DTH performance on *MRE zeolites were encountered regarding product selectivity and longevity. This enables usage in a modified process directing towards high yields of C₅₊ products with very low amounts of aromatics. The aim of the present work is to elucidate this remarkable behavior and elaborate the mechanistic uniqueness compared to common materials. Therefore, we characterized zeolite catalysts of the framework types *MRE, MFI and TON and compared their performances in the conversion of DME. A MFI catalyst was chosen as technically established material, setting the benchmark in reactivity and longevity. TON zeolites are considered to have advantageous structural properties regarding shape selective suppression of aromatics formation thus setting the benchmark in product selectivity. By comparing specific parameters of product selectivity in the case of MFI, TON and *MRE zeolites, peculiarities of the latter zeolite have been identified. Moreover, the influence of varying reaction conditions on the product formation mechanism and longevity of the catalysts has been investigated, determining the most favorable reaction environment to maximize product selectivity and minimize catalyst deactivation.

2. Experimental

2.1. Catalyst materials and preparation

Medium pore zeolites with three different framework types (MFI, *MRE and TON) were employed as catalysts and the main characteristics of the pore channels for the three framework types are listed in Table 1. Zeolite powders in NH₄-form of each framework type were purchased from an industrial supplier. To remove possible impurities, the samples were ion-exchanged three times in 1 M NH₄NO₃ solutions for 2 h at 348 K. After drying for 12 h at 353 K and 1 kPa in a vacuum drying oven, the samples were calcined for 6 h at 823 K (heating rate of 2 K min⁻¹) under static air conditions to obtain the protonated form.

Table 1

Main characteristics of the pore systems for the employed zeolites (data from [25–27]).

Channel characteristics	MFI	*MRE	TON
Dimensionality	3D	1D	1D
Class	Medium	Medium	Medium
Type	10-Ring	10-Ring	10-Ring
Size (Å)	5.4 × 5.6 5.1 × 5.4	5.3 × 5.6	5.5 × 4.5

2.2. Catalyst characterization

Structural properties were analyzed by powder X-ray diffraction (XRD) on a PANalytical X'Pert PRO diffractometer using Cu K α radiation ($\lambda = 0.1541$ nm). The measurements were carried out over 2 h in the 2 θ -range of 5–80°.

Textural properties were determined by Ar-physorption measurements at 87 K on a Quantachrome Autosorb IQ-MP2 in a procedure according to ISO 15901–3:2007 [28]. The samples were outgassed for 12 h at 623 K under vacuum. Isotherms (in the range of relative pressure 0–0.99 p/p_0^1) were used to calculate the specific surface with the BET model (accounting for Rouquerol criteria) [29,30], internal and external surface with the t -plot method and micropore volume by a non-localized density functional theory (NLDFT) kernel.

Particle morphology was investigated by scanning electron microscopy (SEM). SEM images were generated on a Zeiss Gemini SEM 500 with thermal Schottky field emitter cathodes.

Chemical composition was studied by the following characterization techniques: Elemental analysis was determined by using inductively coupled plasma optical emission spectroscopy (ICP-OES) on an Agilent 725 ICP-OES spectrometer. A mixture of 6 mL HNO₃ (65%), 2 mL HCl (30%) and 1 mL HF (40%) (Suprapur®, Merck) was used for microwave digestion of the powder samples. ²⁹Si and ²⁷Al MAS NMR measurements were conducted on a JEOL JNM-ECZ400R spectrometer, equipped with a 9.4 T Oxford cryo magnet, using a 3.2 mm Automas Solid State Probehead. ²⁹Si MAS NMR spectra were recorded at a resonance frequency of 79.45 MHz with a sample spinning frequency of 15 kHz. 4096 scans were accumulated upon $\pi/2$ single pulse excitation with 0.9 s pulse width and 10 s recycle delay. ²⁷Al MAS NMR spectra were recorded at a resonance frequency of 104.20 MHz with a spinning frequency of 15 kHz. 6000 scans were accumulated upon a $\pi/2$ single pulse excitation with 2 s pulse width and 2 s recycle delay. The ²⁹Si chemical shifts were calibrated relative to TMS (tetramethylsilane) and Q₈M₈ (Octakis(trimethylsilyloxy)silsesquioxane) as secondary standard ($\delta = 12.5$ ppm, low-field signal). The ²⁷Al chemical shifts were calibrated relative to potassium aluminum sulfate KAl(SO₄)₂•12 H₂O ($\delta = 0$ ppm).

The acidic character of the catalysts was investigated by FTIR of adsorbed pyridine in a setup, as described in previous reports [31]. The measurements were performed in transmission mode with a Tensor 27 FTIR spectrometer (Bruker) in an in-house made heatable and evacuable reaction cell with water-cooled CaF₂ windows. Prior to the measurements, unsupported wafers of compressed catalyst ($r = 1$ cm, $m = 50$ mg) were outgassed for 1 h at 673 K (heating rate of 10 K min⁻¹) under vacuum, followed by cooling to room temperature. At 473 K, a spectrum of the unloaded sample was recorded to eliminate background signals later. Dried pyridine with Ar as carrier gas (60 mL min⁻¹) was then introduced into the reaction cell until the surface of the sample was saturated. After evacuation of excess gas phase, the reaction cell was heated to 673 K. Then, FTIR spectra were recorded in steps of 50 K. Background signals were subtracted from the IR spectra of pyridine-adsorbed samples at 523 K. The peaks at 1545 cm⁻¹ and 1455 cm⁻¹ were used to calculate the concentration of Brønsted and Lewis acid sites, respectively, according to the equation of Emeis [32].

2.3. Catalytic tests

The catalytic experiments were performed in a continuously operating laboratory plant with a stainless steel tubular fixed-bed reactor (*i. d.* = 12 mm). Gas flows were dosed into the reactor by calibrated thermal mass flow controllers from Wagner-Bronkhorst. Before filling the reactor, the protonated zeolite samples were pressed, crushed and sieved to 224–300 μ m fractions. To ensure minimal temperature gradients, prevent channeling and avoid problems with axial dispersion throughout the catalytic-bed, the catalyst was diluted with inert silicon carbide (SiC, 100–180 μ m sieve fraction) in a catalyst/SiC mass ratio of 1:10. A coaxially movable thermocouple inside the reactor was used to

check isothermal conditions ($\Delta T < 2$ K). Catalyst mass depends on the desired weight hourly space velocity (*WHSV*, defined as mass flow rate of DME divided by the mass of catalyst in the reactor), because a constant mass flow rate of $0.5 \text{ g}_{\text{DME}} \text{ h}^{-1}$ was set for all experiments. Before each experiment, the reactor was heated to reaction temperature in a flow of $80 \text{ mL min}^{-1} \text{ N}_2$. Then, under the same gas flow, the system pressure is adjusted by a manually controlled pressure regulating valve. To start the experiment, a gas mixture of DME and N_2 ($x_{\text{DME}} = 5\%$) was fed into the reactor.

The reactor effluent was transferred to a heated line (453 K), where a partial stream was fed into an online gas chromatograph for analysis of the reaction products. Measurements were carried out every hour. An Agilent 7890B gas chromatograph equipped with a HP-PLOT/Q capillary column (Agilent 19095 P-Q04) and coupled with a flame ionization detector (FID) was used for the quantification of products (hydrocarbons) and reactants (DME and methanol). Additionally, a combination of three HayeSep Q columns (Agilent CP1305) plus one MolSieve 5 Å column (Agilent CP1306) coupled with a thermal conductivity detector (TCD) was used for the quantification of H_2 , N_2 , CO and CO_2 .

The remaining effluent stream was collected in a cold trap cooled to 77 K with liquid N_2 . Sampling started at the beginning of the experiment at 100% conversion until a conversion of 40% was reached. This interval is defined as a “catalyst life cycle” in the following, forming the basis for the calculation of the life cycle yield (*LCY*). Thereafter, at lower conversion consecutive reactions, such as dehydrogenation of coke components on the catalyst with reactants resulting in increased methane formation, became visible in some cases [33]. Afterwards, the products of the cold trap were slowly defrosted to a temperature of 278 K, so that the volatile components evaporated and the hydrocarbon products with five or more C atoms (C_{5+}) plus water remained liquid in the collecting vessel of the cold trap. After phase separation, the organic phase was analyzed in a Reformulyzer M4 (PAC) with a multi-dimensional PIONA gas chromatography method in compliance with ISO 22854:2021 [34]. A more detailed description of the product analysis procedure is given in the [Supplementary Material](#).

3. Results and discussion

3.1. Catalyst properties

The main characteristics of the three different zeolite framework types are listed in [Table 2](#). Si/Al ratios of 40.2, 73.5 and 50.4 were measured for MFI, *MRE and TON, respectively.

Ar-physorption isotherms are shown in [Fig. S1](#) of the [Supplementary Material](#). BET surface areas of 459, 195 and $228 \text{ m}^2 \text{ g}^{-1}$ are slightly above literature data for comparable materials ($433 \text{ m}^2 \text{ g}^{-1}$ for MFI (Si/Al ≈ 40) [35], $148 \text{ m}^2 \text{ g}^{-1}$ for *MRE (Si/Al ≈ 72) [24] and $196 \text{ m}^2 \text{ g}^{-1}$ for TON (Si/Al ≈ 50) [15]). The deviation can be explained by the use of Ar as adsorbate, as advised by IUPAC [36], whereas N_2 was used in the literature reports. The external/internal surface ratio of 0.18 for MFI is lower compared to 0.27 for TON and 0.59 for *MRE. In line with this, the micropore volume of $0.22 \text{ cm}^3 \text{ g}^{-1}$ for MFI is higher compared to 0.10

Table 2
Main characteristics of the employed zeolites.

	MFI	*MRE	TON
Si/Al ratio (mol mol^{-1}) ^a	40.2	73.5	50.4
BET area ($\text{m}^2 \text{ g}^{-1}$)	459	195	228
External/internal surface ^b	0.18	0.59	0.27
Micropore volume ($\text{cm}^3 \text{ g}^{-1}$) ^c	0.22	0.07	0.10
Brønsted acid sites ($\mu\text{mol g}^{-1}$) ^d	235	97	170
Lewis acid sites ($\mu\text{mol g}^{-1}$) ^d	37	24	22

^a ICP-OES.

^b *t*-plot.

^c NLDFT.

^d Pyridine FTIR.

$\text{cm}^3 \text{ g}^{-1}$ for TON and $0.07 \text{ cm}^3 \text{ g}^{-1}$ for *MRE. These observations show a higher proportion of accessible intracrystalline volume inside the MFI framework structure compared to TON and *MRE. This is likely due to the three-dimensional pore system of MFI with linked channels versus the unidirectional one-dimensional TON and *MRE pores.

FTIR spectra of pyridine adsorbed at 523 K are depicted in [Fig. S2](#). The Brønsted acid site density was calculated as $235 \mu\text{mol g}^{-1}$ for MFI, $170 \mu\text{mol g}^{-1}$ for TON and $97 \mu\text{mol g}^{-1}$ for *MRE from the peaks at 1545 cm^{-1} . This order is consistent with the Si/Al ratio of the materials. The Lewis/Brønsted acid site ratio of 0.25 for *MRE is high compared to 0.16 for MFI and 0.13 for TON, indicating a high proportion of Lewis acidic Al in non-framework positions (extra framework Al, EFAl).

Representative SEM images of the catalyst samples are shown in [Fig. 1](#). The MFI particles are aggregates in the range of 0.1–1 μm , composed of slaty, irregular crystals in the range of 20–200 nm. Depending on the material synthesis, different morphologies of MFI crystals can be formed, which have been classified by Jacobs and Martens [37]. The MFI morphology shown in [Fig. 1](#), corresponds to the class of spherulitic agglomerates. The *MRE sample revealed a morphology of irregular aggregates in the range of 0.5–2 μm , assembled by intergrowth of mainly rod/needle and plate shaped crystals with <100 nm length. Similar observations on *MRE crystal morphology have been published previously [15,38]. The SEM images of TON show a morphology of columnar aggregates in the range of 0.1–2 μm , formed by uniformly unidirectional intergrown rod/needle shaped crystals with <100 nm length. This is consistent with previous reports and is considered a typical morphology for zeolite framework types with one-dimensional 10 ring pore systems [15,39].

XRD diffractograms of the three zeolites are depicted in [Fig. 2](#). The patterns expose a high degree of crystallinity for all samples. Furthermore, the patterns match the reported structures of orthorhombic MFI [35], *MRE [15,26] and TON [15,27]. No impurities of the MFI and *MRE zeolites could be observed. The small peak at approximately $21.7^\circ 2\theta$ in the TON diffractogram indicates a minor cristobalite impurity [27, 40].

^{29}Si MAS NMR spectra of highly siliceous zeolites are expected to reveal $\text{Q}_4[\text{Al}_0]$ signals in the range of -110 to -117 ppm, crystallographically corresponding to distinct Si sites with varying Si-Si distances and Si-O-Si angles [41]. The insertion of Al in the framework broadens the peaks and draws some intensity to the $\text{Q}_4[\text{Al}_1]$ resonance around -105 ppm. SiOH type structural defects ($\text{Q}_3[\text{Al}_0]$) can be observed at -102 ppm. Orthorhombic [Si-O]-MFI was reported to reveal 12 resonances in an asymmetric arrangement, assigned to the different T-sites of the unit cell [42,43]. Due to the Si/Al ratio of 40, the MFI sample of this work is expected to be in the orthorhombic phase [44]. The broad overlain total $\text{Q}_4[\text{Al}_0]$ signal of MFI presented in [Fig. 3](#) (top) comprises a main peak at -112.2 ppm with a shoulder at -115.3 ppm. Furthermore, the broad signal at lower shift indicates the presence of Al ($\text{Q}_4[\text{Al}_1]$ signal at -105.5 ppm) and SiOH ($\text{Q}_3[\text{Al}_0]$ signal at -101.5 ppm). Similar behavior is widely reported in the literature [45,46]. For TON, ^{29}Si MAS NMR spectra of dealuminated materials were reported to reveal four symmetrical peaks with relative intensities in the ratio of 2:1:1:2, which represent the four symmetrically inequivalent T-sites of the unit cell [47,48]. However, the total $\text{Q}_4[\text{Al}_0]$ signal of the TON sample is not symmetrical, as shown in [Fig. 3](#) (top). This might be caused by a non-uniform distribution of Al over the inequivalent T-sites [49]. The broad and weak signal beginning at -100 ppm is formed by the combination of $\text{Q}_4[\text{Al}_1]$ and $\text{Q}_3[\text{Al}_0]$ peaks. For *MRE, no ^{29}Si NMR spectra of highly siliceous samples with clearly defined $\text{Q}_4[\text{Al}_0]$ signals of different T-sites could be found in the literature. The highly symmetric peak at -113 ppm, which was observed for the *MRE sample, coincides with reports of Al-containing *MRE zeolites in the literature [50,51]. The lower signal intensity at -105 ppm in relation to the main peak indicates a lower Al content of the *MRE sample compared to MFI and TON.

The ^{27}Al NMR spectra in [Fig. 3](#) (bottom) show the typical signals of

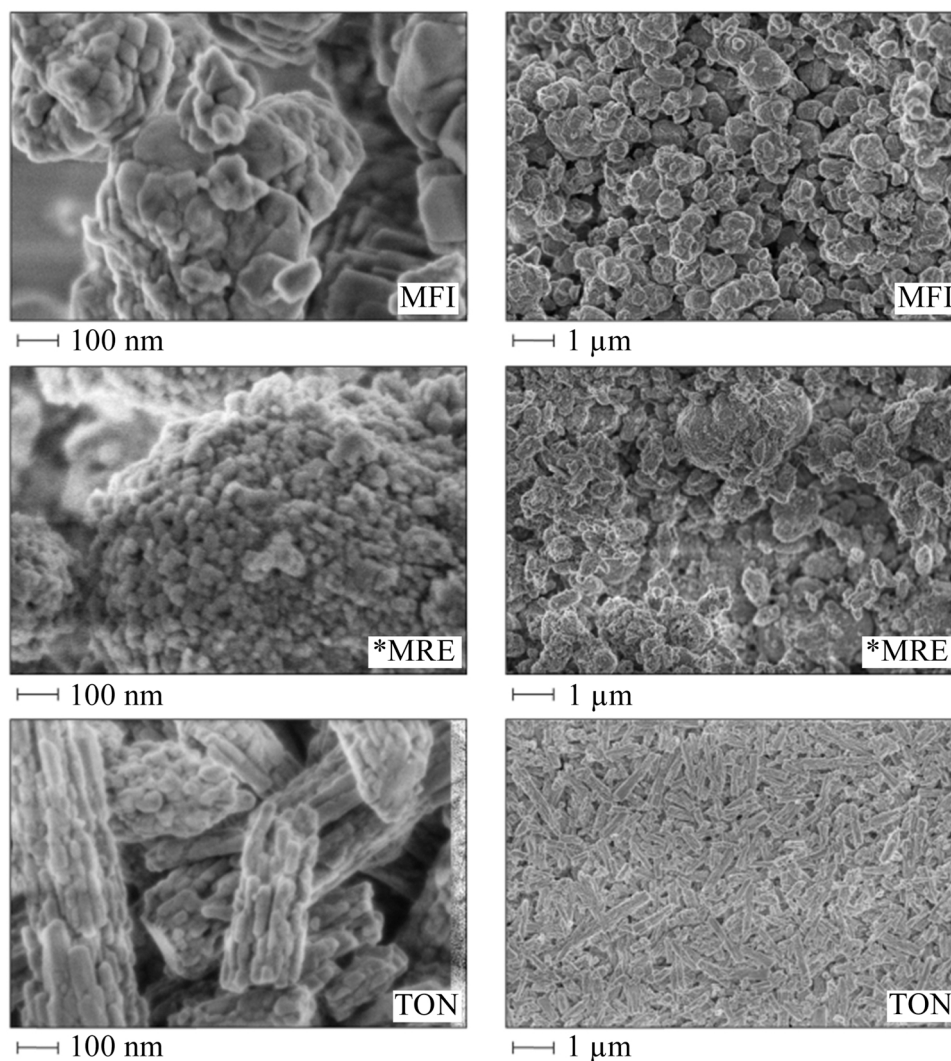


Fig. 1. SEM images of the zeolites.

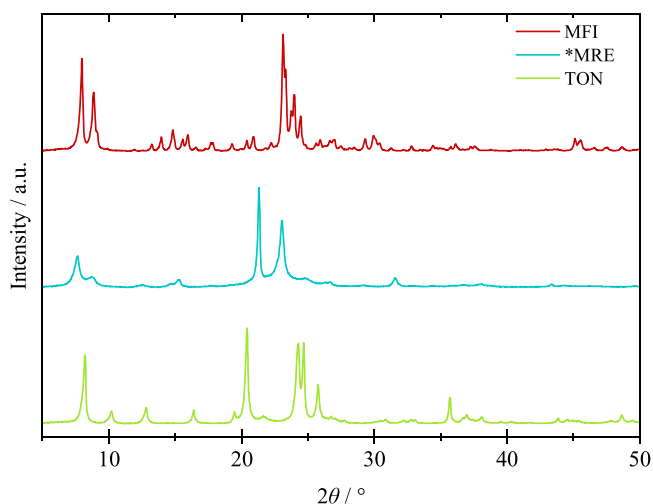


Fig. 2. XRD patterns of the zeolites.

tetrahedrally coordinated framework Al at ~ 55 ppm and octahedrally coordinated extra framework Al (EFAL) at ~ 3 ppm. The signal intensity of the *MRE sample at ~ 55 ppm was lower compared to MFI and TON,

which can be attributed to the lower Al content of the material. Furthermore, it is clearly noticeable, that the content of EFAL in *MRE exceeds the EFAL contents in MFI and TON. This is in good agreement with the comparatively high content of Lewis acid sites of the *MRE sample, probably caused by EFAL, which was detected by pyridine adsorption measurements (Table 2). The high content of EFAL could be due to the disordered *MRE framework, as indicated by the symbol *, coming along with more lattice defects compared to the ordered structures.

3.2. Catalytic tests

3.2.1. Catalytic performance of the zeolites MFI, *MRE and TON

The DME conversion versus the cumulative conversion capacity for zeolites MFI, *MRE and TON is shown in Fig. 4. Experiments were carried out at 673 K and 100 kPa DME partial pressure. Due to a strongly varying DTH activity of the materials, catalyst loading in terms of *WHSV* was individually adjusted (6.0 h^{-1} for MFI, 1.5 h^{-1} for *MRE and 0.3 h^{-1} for TON). Thus, an initial conversion of 100% could be maintained for at least 24 h TOS in all experiments of this series. The highest cumulative conversion capacity was observed for MFI, which is known for its longevity in methanol or DME conversion to hydrocarbons when compared to other zeolites [22]. The one-dimensional zeolites *MRE and TON deactivated more rapidly, while *MRE vastly outperformed TON. This observation deviates from previously published reports,

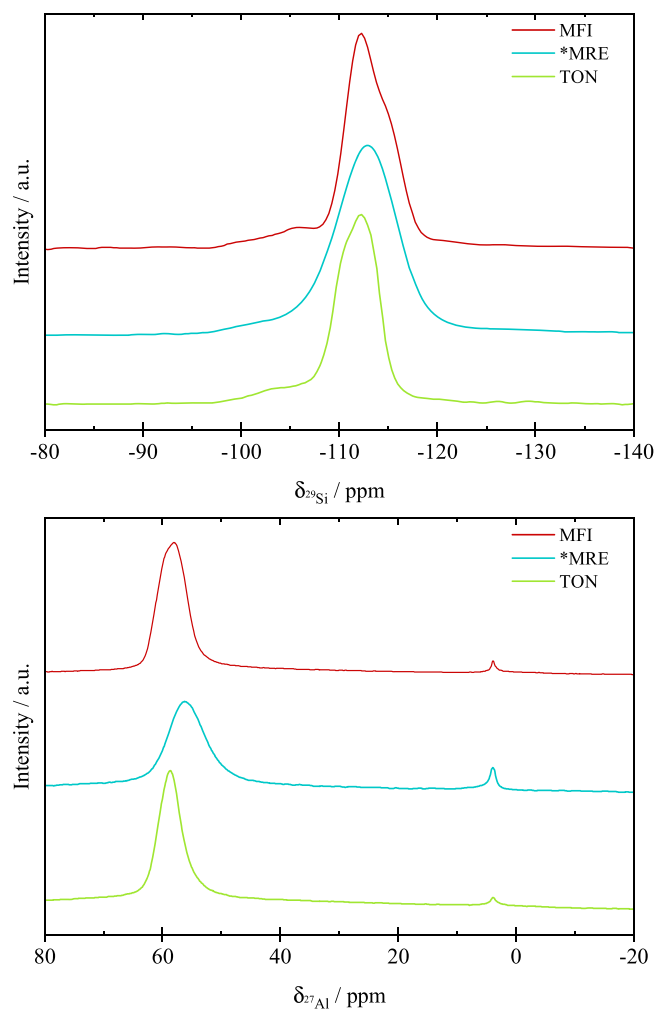


Fig. 3. ^{29}Si (top) and ^{27}Al (bottom) MAS NMR spectra of the zeolites.

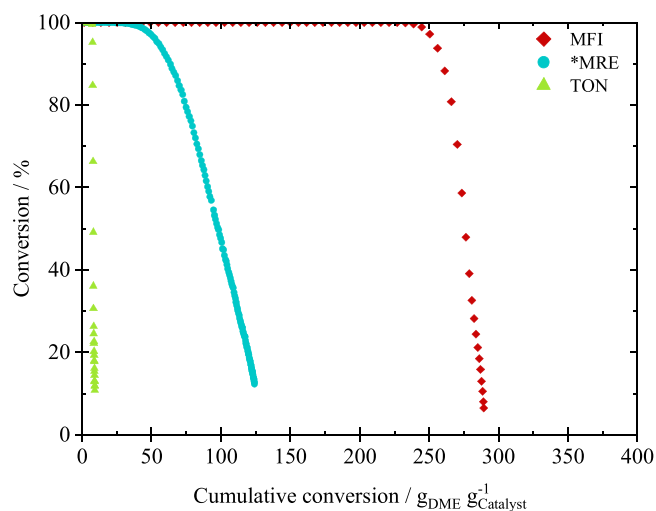


Fig. 4. DME conversion versus the cumulative conversion capacity for MFI, *MRE and TON zeolites (reaction conditions: $T = 673\text{ K}$, $p_{\text{DME}} = 100\text{ kPa}$, $\text{WHSV} = 6.0\text{ h}^{-1}$ (MFI), 1.5 h^{-1} (*MRE) and 0.3 h^{-1} (TON)).

where a similar resistance to deactivation for *MRE and TON type catalysts was stated [15,23]. According to the cumulative conversion capacity at 100% DME conversion, in combination with the respective

WHSV, the activity of the materials can be ranked in the order $\text{MFI} > \text{*MRE} > \text{TON}$. The higher activity of MFI compared to *MRE and TON can be explained by the different dimensionality of the pore systems. The diffusion of reactants into the pores, the movement of the molecules through the pores and the release of reaction products from the pores is facilitated by the three-dimensional structure of the MFI pore channels with intracrystalline junctions and openings across the entire outer surface. In contrast, the non-interpenetrating pore channels of *MRE and TON run longitudinally through the entire crystal, so that diffusion of guest molecules occurs only alongside a single channel. The slightly different pore diameters of *MRE ($5.3 \times 5.6\text{ \AA}$ [26]) and TON ($5.5 \times 4.5\text{ \AA}$ [27]) are probably a major reason for the different activities of these two materials with the same dimensionality.

Stability of the materials can be analogously explained. For instance, Guisnet et al. [52,53] showed that the lifetime of zeolites in catalytic reactions for the conversion of hydrocarbons is linked to the dimensionality of the pore system. Accordingly, zeolite structures with one-dimensional pore systems are considered to be particularly sensitive to deactivation due to the blockage of entire pore channels. A small coke deposit in a pore channel may be sufficient to inhibit the activity of all active sites within the channel. Since coke formation and accumulation occurs preferably near the crystal outer surface [54], such deposits can directly block the entire channel in the case of a one-dimensional structure. In contrast, coke deposits in zeolites with a three-dimensional pore system without “trap-cages” may only block individual acid sites or small sections of the pore systems thus avoiding accumulation. Therefore, only small sections within the pore system initially deactivate and can be bypassed by redirecting intramolecular diffusion. In such zeolites, to whom the framework type MFI is allocated, the blockage of entire channels occurs only in the highly coked state and may be attributed to the formation of large, bulky deposits on the outer surface of the crystal [53,55,56].

3.2.2. Product yields for the zeolites MFI, *MRE and TON

The yield of C_{5+} hydrocarbons versus DME conversion for the three catalysts is depicted in Fig. 5. The MFI zeolite revealed a relatively high and constant C_{5+} yield between 55% and 60% at full conversion. Below 100% reactant conversion, a linear decrease of C_{5+} yield was observed. In the case of the *MRE and TON zeolite, the C_{5+} yield increased constantly in the beginning of the experiments at 100% conversion. The maximum C_{5+} yield of 60% for *MRE and 61% for TON was reached below complete reactant conversion, at 92% and 95%, respectively. Afterwards, in both cases the C_{5+} yield decreased with a slightly convex

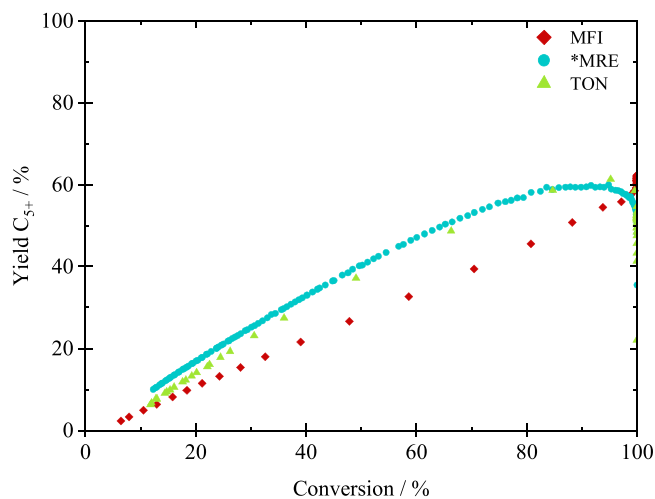


Fig. 5. Yield of C_{5+} hydrocarbons versus DME conversion for MFI, *MRE and TON zeolites (reaction conditions: $T = 673\text{ K}$, $p_{\text{DME}} = 100\text{ kPa}$, $\text{WHSV} = 6.0\text{ h}^{-1}$ (MFI), 1.5 h^{-1} (*MRE) and 0.3 h^{-1} (TON)).

curvature. The corresponding data for the fractions of methane, ethane, ethene, propane, propene, butanes and butenes are shown in the [Supplementary Material \(Fig. S3\)](#).

Volume group type fractions of the liquid C₅-C₁₁ product phase during a catalyst life cycle of the zeolites MFI, *MRE and TON, as defined in Chapter 2.3, are depicted in [Fig. 6](#). In the C₅ and C₆ fractions a high content of paraffins, especially branched *iso*-paraffins, was detected in the case of the MFI catalyst. Regarding C₇₊ components, an increasing content of aromatics was formed. The olefin content was consistently low, with only cyclic olefins being formed from C₈ upwards. In contrast, the *MRE catalyst led to a consistently high olefin content in all fractions and *iso*-olefins dominated the olefin fraction. Only a small content of paraffins and even less aromatics were detected in the liquid product phase. The TON catalyst gave a fairly balanced ratio of paraffins, olefins and aromatics. For low carbon numbers, the liquid product spectrum was dominated by olefins and paraffins. With increasing carbon numbers their proportion decreased in favor of aromatics. The volume fraction of hydrocarbons with 12 or more C-Atoms (C₁₂₊) was below 1% for all three zeolites in the PIONA group type analysis.

By combination of the PIONA group type analysis data for the product group C₅₊ with the average values of the C₁-C₄ yields, the yield of all products (C₁-C₁₁) was calculated for the three catalysts ([Fig. 7](#)). For MFI, the highest yield was achieved in the case of C₄ products. Paraffins were the dominant product group (52%), followed by almost similar proportions of olefins (26%) and aromatics (22%). For *MRE, C₄ compounds also represented the largest product fraction and olefins were by

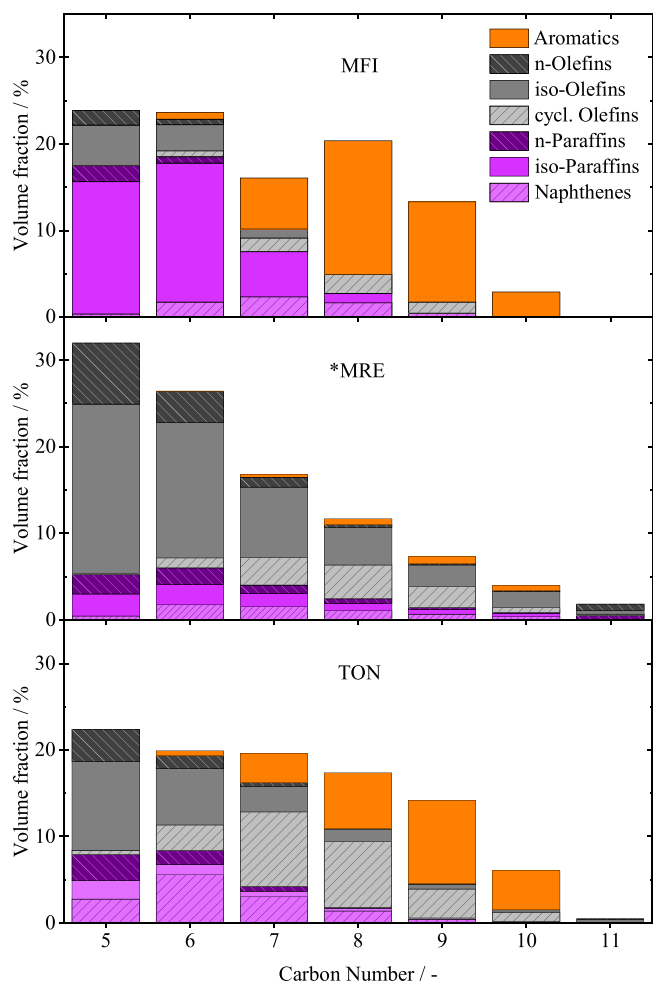


Fig. 6. Volume group type fractions of the liquid C₅-C₁₁ product phase for the zeolites MFI (top), *MRE (middle) and TON (bottom). PIONA group type analysis in compliance with ISO 22854:2021 [34].

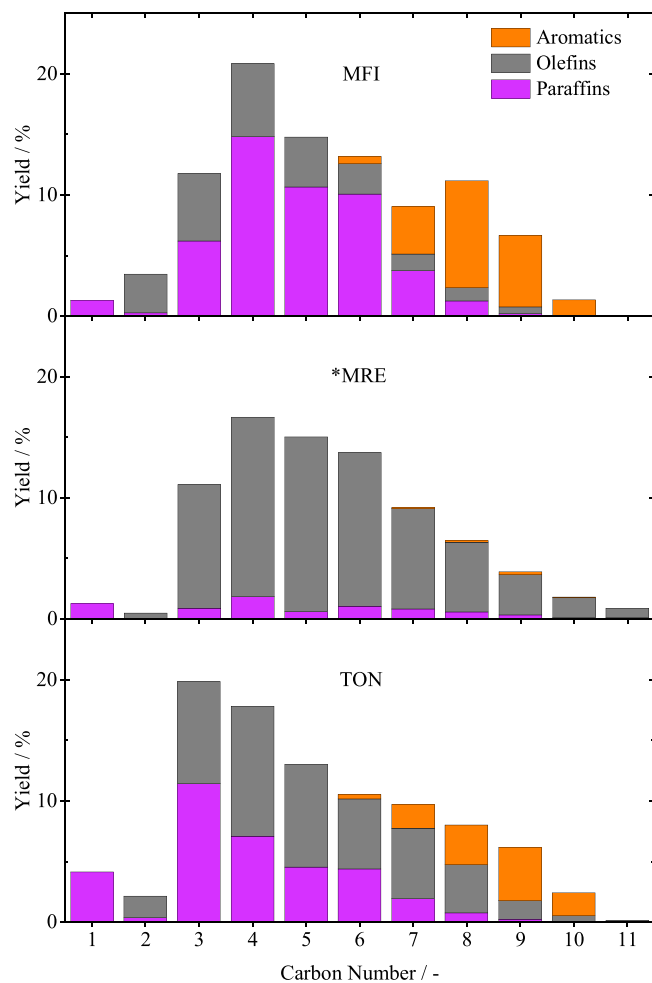


Fig. 7. Yields of C₁-C₁₁ products for the zeolites MFI (top), *MRE (middle) and TON (bottom).

far the major product group (90%). Small amounts of paraffins (9%) and even smaller amounts of aromatics (<1%) were formed. The main product fraction in the case of TON was the C₃ fraction. Olefins were the largest hydrocarbon fraction (50%), followed by paraffins (37%) and aromatics (13%) with significantly higher proportions compared to *MRE. Conversion capacity, yield of liquid C₅₊ phase as well as C₅₊ mass fractions for a catalytic life cycle of all catalysts are listed in [Table 3](#). The high olefin formation of the *MRE and TON zeolites seems to cause the rising selectivity to C₅₊ products with increasing deactivation, which is shown in [Fig. 5](#). Simonetti et al. [57,58] showed by studying the chain growth of light olefins using DME as methylation reagent, that for products in the chain length range <C₈, olefin cracking has the highest activation barrier and thus the lowest reaction rate compared to methylation and hydride transfer. Guisnet et al. [53] reported that for zeolites with unequal acid strength within the pore system, the strongest, most active centers will deactivate first, thereby reducing the rate

Table 3
Performance parameters for the zeolites MFI, *MRE and TON.

Catalyst	Conversion capacity (g _{DME} g _{Catalyst} ⁻¹)	LCY _{C5+} (g _{C5+} g _{Catalyst} ⁻¹)	Mass fractions C ₅₊ phase		
			Paraffins (%)	Olefins (%)	Aromatics (%)
MFI	279	102	41.5	15.8	42.6
*MRE	105	41	7.6	91.1	1.3
TON	8	3	21.5	50.4	28.1

of reaction steps with high activation barrier, like the cracking of higher olefins in this case. This explains the increased formation of C_{5+} olefins during deactivation of *MRE and TON zeolites.

Analysis of the yields, either online or offline after collection of the product mixtures, indicate major differences in product formation for the three zeolites. As widely reported in the literature, DTH product formation on zeolites occurs via the dual cycle model [12]. The so-called Hydrogen-Transfer-Index (HTI_{C_i} , defined as the ratio of saturated products to total products of carbon number i) is a qualitative indicator of the hydride transfer during the DTH reaction [59]. Hydride transfer between olefins is mandatory for the formation of paraffins and aromatics in the reaction network. An indicator for the formation of products via the aromatic cycle of the dual cycle model is the formation of ethene. Ethene is inherently linked to alkylation/dealkylation of aromatics and can be excluded as cracking product of higher olefins [60]. In addition, methylation activity of ethene in the olefin cycle of the dual cycle model is very low compared to propene and butenes [60]. Since the oligomerization of light olefins is suppressed in the presence of methanol/DME [61,62], the conclusion that ethene leaves the reactor without a subsequent reaction is valid. In contrast, due to steric constraints in medium pore zeolites, propene formation differs, from a mechanistic point of view, from cracking reactions of polymethylated aromatics [63,64]. Accordingly, for 10-ring zeolite framework types, propene is considered a key component of the olefin cycle which is formed mainly from olefin methylation and interconversion. Consequently, the C_3/C_2 product ratio can be considered as an indicator for the intensity of the olefin cycle compared to the aromatics cycle.

Fig. 8 depicts the HTI_{C_3} and the C_3/C_2 ratio versus DME conversion. It is clearly visible, that at high conversion the HTI_{C_3} of the *MRE catalyst was comparatively low, whereas the C_3/C_2 ratio was exceptionally high. This means that the hydride transfer in the HCP is low and product formation hardly occurs via alkylation/dealkylation of aromatics. Based on these indicators, the conclusion can be drawn, that the aromatic cycle is suppressed on *MRE under the given conditions, which is also in accordance with the measured yields. These observations deviate from previously published data on *MRE type catalysts, where substantial amounts of aromatics, high HTI values and low C_3/C_2

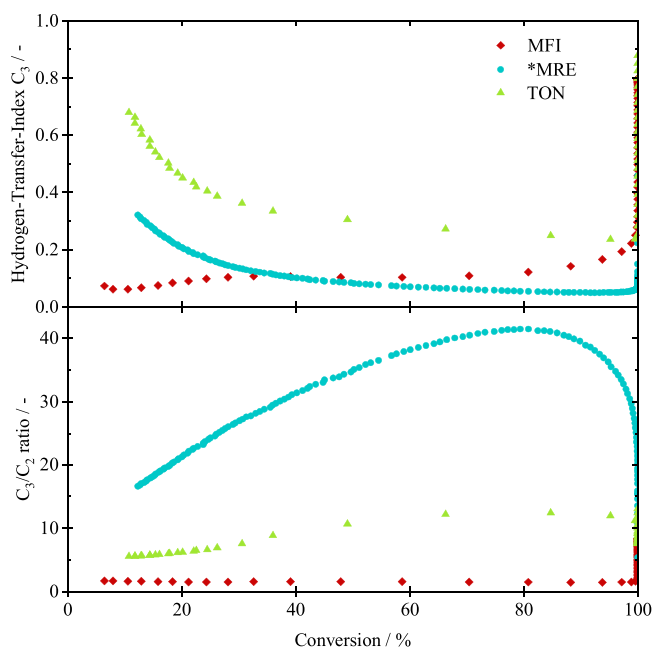


Fig. 8. HTI_{C_3} (top) and C_3/C_2 ratio (bottom) versus conversion during the DTH reaction on MFI, *MRE and TON zeolite catalysts (reaction conditions: $T = 673$ K, $p_{DME} = 100$ kPa, $WHSV = 6.0$ h $^{-1}$ (MFI), 1.5 h $^{-1}$ (*MRE) and 0.3 h $^{-1}$ (TON)).

product ratios were reported [23]. These differences are probably due to different reaction conditions, which will be considered in Chapter 3.2.3. Catalyst deactivation is associated with a reduction of active catalyst mass in reactor. This implies a reduction of the contact time (contact time τ_0 , defined as mass of catalyst in the reactor divided by the total gas volume flow in the reactor) and is expected to cause a decrease of HTI_{C_3} with increasing catalyst deactivation [59]. However, this effect is only observed for the MFI zeolite, whereas the *MRE and TON zeolites behave differently with an increasing HTI_{C_3} during deactivation.

Since hydride transfer is a bimolecular reaction step in the HCP reaction network, the reaction rate is expected to decrease with increasing $WHSV$ for a given catalyst. Despite a four times higher $WHSV$, significantly higher HTI_{C_3} values were measured for the MFI catalyst at high conversion, compared to *MRE. The high hydride transfer rate explains the large fractions of paraffins and aromatics in the product spectra while the very low C_3/C_2 ratio indicates enhanced product formation via cracking of methylated aromatics.

For TON, the HTI_{C_3} was higher compared to the two other zeolites. Besides the structural properties of the TON framework, the comparatively high τ_0 may have a noticeable impact on the hydride transfer during the reaction. Resulting from the high hydride transfer rate, high amounts of aromatics are formed, whose mobility is severely restricted in the narrow TON pore channels. Polymethylated benzenes reside inside the TON crystal and block the channels, which explains the rapid deactivation and low cumulative conversion capacity of the material [15–17]. The C_3/C_2 ratio of TON is in between MFI and *MRE indicating that, despite the potentially high aromatics formation rate, dealkylation of aromatics is limited due to steric constraints of the zeolite framework. A significant part of the products is thus formed via the olefin cycle. Thereby, the performance of the TON catalyst, yielding a product composition between the two extremes *MRE (dominant olefin cycle) and MFI (dominant aromatic cycle), can be explained.

3.2.3. Variation of reaction conditions

The three catalysts were tested with varying temperature, DME partial pressure and $WHSV$ to determine the influence of reaction conditions on the DTH reaction network and to investigate practical aspects like effects on product selectivity or catalyst lifetime. The conditions for experiments presented in Sections 3.2.1 and 3.2.2 ($T = 673$ K, $p_{DME} = 100$ kPa, $WHSV = 6.0$ h $^{-1}$ for MFI, 1.5 h $^{-1}$ for *MRE and 0.3 h $^{-1}$ for TON) represent the base case for this test series. Starting from these values, one parameter was varied in each case. The cumulative conversion versus C_{5+} product yield (top) and C_3/C_2 ratio versus HTI_{C_3} (bottom) of the MFI, *MRE and TON catalysts are shown in Fig. 9. C_{5+} product yield, C_3/C_2 ratio and HTI_{C_3} are given as average values for the period from the beginning of the experiment until the point of 40% DME conversion (see above). Further data on this experimental series are shown in the Supplementary Material.

The cumulative conversion for the MFI catalyst decreased with increasing temperature, while for *MRE and TON a maximum cumulative conversion was achieved at 673 K under the given conditions. The initial DTH conversion in the case of the *MRE catalyst at 648 K was below 40% (Fig. S4) and thus too low for the criteria of the evaluation shown in Fig. 9. The maximized cumulative conversion in each case should be closely associated with a minimized formation of deactivating species. Formation of such species occurs through manifold pathways driven by reactants [65–67], interactions of reactants and HCP products [68,69] or HCP products alone [70,71]. This can result in countervailing deactivation mechanisms, especially depending on the temperature. At low temperatures, a decreasing cracking rate of olefins and dealkylation rate of aromatics favors the formation of bulky molecules within the zeolite pores. Additionally, the built-up of the autocatalytic HCP is slowed down, resulting in a prolonged induction period [72]. On the other hand, coking reactions, in which the oxygenate reactants act as precursors seem to proceed preferentially at higher temperatures [67]. Based on early observations of Hutchings et al. [65], a mechanism of

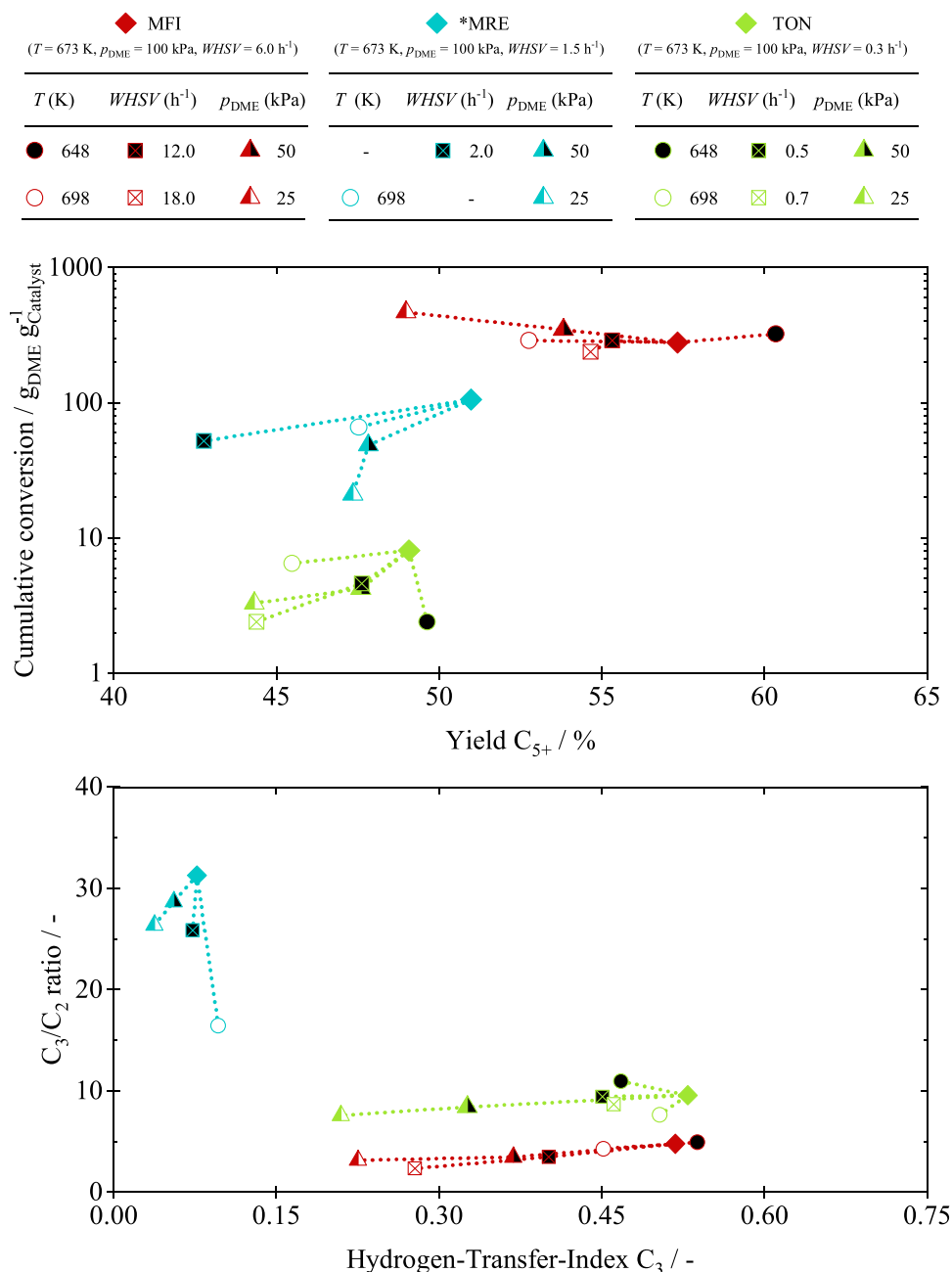


Fig. 9. Cumulative conversion versus C_{5+} product yield (top) and C_3/C_2 ratio versus HTI_{C_3} (bottom) of the zeolites MFI, *MRE and TON for varying reaction conditions. The diamond symbols represent the base case conditions for each catalyst ($T = 673 \text{ K}, p_{\text{DME}} = 100 \text{ kPa}, \text{WHSV} = 6.0 \text{ h}^{-1}$ for MFI, 1.5 h^{-1} for *MRE and 0.3 h^{-1} for TON), other symbols refer to the variation of one parameter.

coke formation related to formaldehyde formation by hydride transfer of chemisorbed methanol was proposed lately [66,67,73,74]. A direct disproportionation of the methylation agent DME to form formaldehyde is not possible. However, methanol is constantly generated during the catalytic reaction, by DME methylation or hydrolysis of DME [11]. Formaldehyde can act as precursor for strongly adsorbed oxygen-containing surface species, which are converted to aromatics with increasing time on stream [67]. Aromatics formed by this mechanism will not easily desorb from the active sites of the catalyst, causing deactivation by site blocking [67]. A temperature dependency of this process was observed and higher temperatures led to higher amounts of coke deposits [67]. For MFI, strongly chemisorbed aromatics can enhance product formation via alkylation/dealkylation according to the aromatic cycle, which explains the decreasing C_3/C_2 ratio. As more

aromatics are retained on the active sites inside the catalyst at higher temperatures, C_{5+} product yield and cumulative conversion decrease because of faster deactivation. This assumption is underlined by an increased C_1 yield, known as a by-product of coke formation from oxygenates, at higher temperatures (Table S1). In contrast, the formation of bulky, but mobile, molecules at lower temperatures seems to have only a slight negative effect in the three-dimensional MFI pore system with spacious channel intersections. For *MRE, a decrease of the cumulative conversion and C_{5+} product yield were observed together with a drastically reduced C_3/C_2 ratio and slightly increased HTI_{C_3} by increasing the temperature from 673 K to 698 K. These findings suggest an increased formation of aromatics, as well as an increased contribution of the aromatic cycle to the reaction. Similar observations were published by Zhang et al. [24] for temperatures in the range of

723–973 K. The enhanced formation of products via the aromatic cycle could be attributed to aromatics produced by the oxygenate coking mechanism. It can be assumed that, due to the steric constraints of the *MRE framework, the formation of transition states for the dealkylation of strongly bound aromatics inside the pore channels are hindered [15]. Therefore, alkylation of these aromatics can rapidly lead to deactivation by pore blockage, which could explain the lower cumulative conversion and lower C_{5+} product yield at higher temperatures. In addition, an increased olefin cracking rate at higher temperatures may affect the C_{5+} yield. Despite the reduced C_3/C_2 ratio, the olefin cycle appears to remain dominant over the aromatic cycle in comparison to the other zeolites studied within this work. As a result of the high olefin concentration in the HCP inside the *MRE pores, the formaldehyde formed during oxygenate hydride transfer may react with olefins to form dienes. These in turn are assumed to be highly reactive for cyclization with subsequent hydride donation resulting in the formation of aromatics [75]. Thus, this mechanism could contribute to both, the reduced C_3/C_2 ratio and the increased HTI_{C_3} . For TON, the C_3/C_2 ratio decreased at higher temperatures, whereas the HTI_{C_3} showed a maximum at 673 K. The little cumulative conversion at 648 K can be explained by reduced aromatic dealkylation at lower temperatures (higher C_3/C_2 ratio), resulting in more bulky molecules (higher C_{5+} yield) which block the narrow pore channels of the zeolite. The low HTI_{C_3} can be linked to the fast deactivation, which shortens the average τ_0 by fast reduction of active catalyst mass [59]. With increasing temperature, the aromatic dealkylation rate increases, which reduces pore blocking (lower C_3/C_2 ratio and C_{5+} yield). But at the same time, the rate of oxygenate hydride transfer, indicated by increasing C_1 yield (Table S1), may increase as well, facilitating the formation of deactivating species according to this mechanism. At 698 K, this disadvantage seems to outweigh the advantages of the increased dealkylation rate, which lowers the cumulative conversion compared to the experiment at 673 K. The low HTI_{C_3} in turn may result from the short average τ_0 .

The impact of varying $WHSV$ on product formation of the different catalysts is more distinct than the impact of temperature variation, since no countervailing effects occur. Increasing $WHSV$ values cause a reduction of τ_0 . Lower τ_0 should reduce the probability of bimolecular reactions like olefin hydride transfer (lower HTI_{C_3}) and most likely favor monomolecular reactions like olefin cracking (lower C_{5+} yield) or dealkylation of aromatics (lower C_3/C_2 ratio and lower C_{5+} yield). These effects should have a positive impact on the longevity of the catalysts, as reaction steps that contribute to the formation of deactivating species are reduced. However, to build up the HCP during the initial phase of the reaction, a critical concentration of autocatalytic species must be generated inside the catalyst bed. The critical contact time $\tau_{0,crit}$ is defined as the contact time needed to build up a HCP concentration where the autocatalytic reaction is dominating the overall reaction rate [76]. The axially position where the accumulation of HCP species begins, depends on the contact time [77]. From there, the HCP may firstly arise in the opposite direction to the reactant flow and the HCP can move later with the flow [77]. If the accumulation of the active species begins early enough in the catalyst bed, the entire catalyst volume is used for the autocatalytic reaction during time on stream. In this case, the cumulative conversion capacity of a catalyst does not change, despite different $WHSV$ values, as observed for MFI at $WHSV$ values of 6.0 h^{-1} and 12.0 h^{-1} . If the accumulation zone of active species shifts towards the end of the catalyst bed due to shorter τ_0 , the entire catalyst volume is probably not used during the autocatalytic phase, since the spatial expansion of HCP formation against flow direction is limited. The phenomenon of an “unused” coke free inlet zone of a deactivated catalyst bed at short τ_0 has been photographically documented by Bleken et al. [78]. In this case, the cumulative conversion capacity of a catalyst decreases with increasing $WHSV$, as observed for MFI at 18.0 h^{-1} , or for TON at 0.5 h^{-1} and 0.7 h^{-1} . A moderately lower cumulative conversion capacity in the case of MFI and a considerable decrease in the case of TON were observed with increasing $WHSV$ at full initial conversion and

these findings are in line with observations of Rojo-Gama et al. [79]. The different behavior may be attributed to the influence of $\tau_{0,crit}$, which was reported to be minimal on MFI and clearly noticeable on TON [76,79]. Catalyst deactivation driven by reactants strongly depends on the influence of $\tau_{0,crit}$, as this is the predominant deactivation mechanism until the HCP is built up and reactant-HCP interactions become dominant. This is underlined by the observation of enhanced methane formation at lower $\tau_0/\tau_{0,crit}$ ratios corresponding to increasing $WHSV$ (Table S2). For very high $WHSV$, τ_0 drops below $\tau_{0,crit}$, so that the initial accumulation of autocatalytic species can no longer occur at complete reactant conversion, as seen for *MRE when the $WHSV$ was increased from 1.5 h^{-1} to 2.0 h^{-1} (Fig. S5). The cumulative conversion capacity of the catalyst was reduced in this case, since the deactivation of the catalyst caused by oxygenate precursors [66,67] is already underway during the slow build up of the HCP. This interpretation is supported by an increased C_1 yield at a $WHSV$ of 2.0 h^{-1} (Table S2). When the $WHSV$ was further increased to 2.5 h^{-1} , the catalytic activity of *MRE was insufficient to build up the HCP. Mainly methane was produced at a very low conversion level (<20%).

Lowering the DME partial pressure at constant $WHSV$ and feed composition can be understood as a reduction of τ_0 , analogous to an increase of $WHSV$ at constant partial pressure. However, as the reduced τ_0 results from an increased flow velocity inside the reactor, DME concentration at the reactor entrance is reduced at lower reactant partial pressure. This leads to a shift in the ratio of primary methylation reactions to secondary HCP interconversions, in favor of the latter. Furthermore, a shortened τ_0 promotes monomolecular secondary reactions like olefin cracking over bimolecular secondary reactions like olefin hydride transfer. The consequences of these effects are represented in the experimental data by a lower C_{5+} product yield, C_3/C_2 ratio and HTI_{C_3} at reduced DME partial pressures. This is completely in line with literature data for MFI zeolites which describe, that at low reactant partial pressure formation of short-chain olefins is promoted and aromatics formation is reduced [22,80,81]. Since the catalytic activity of the MFI zeolite is high enough to compensate for the shortened τ_0 , lower DME partial pressure had a perceptible positive effect on the cumulative conversion capacity of the material by reducing the formation of bulky unsaturated products, which can act as coke precursors. Contrary to a reduction of the $WHSV$ at constant DME partial pressure, the reduction of the DME partial pressure at constant $WHSV$ causes a mitigation of $\tau_{0,crit}$ besides shortened τ_0 , due to the lower DME concentration [76]. This relationship is particularly supported by the fact that for *MRE the HCP was build up at complete conversion for each level of DME partial pressure. At both 25 and 50 kPa DME partial pressure, τ_0 falls below the value of operating at 100 kPa DME partial pressure and $WHSV$ of 2.5 h^{-1} where, as shown above, the catalytic activity of the zeolite was insufficient to build up the HCP. Since bimolecular hydride transfer and subsequent reaction steps of aromatics formation generally appear to be very weak for *MRE zeolites, the combined effects of shortened τ_0 and low DME concentration seem to have only a minor impact on the longevity of the catalyst. Rather, decreasing $\tau_0/\tau_{0,crit}$ ratio appears to accelerate reactant-induced deactivation, mitigating the cumulative conversion at lower DME partial pressure levels. For the TON zeolite, lowering the DME partial pressure has the same effect on the cumulative conversion as for *MRE.

4. Conclusions

The catalytic DTH conversion on zeolites with the framework types MFI, *MRE and TON revealed notable different shape selectivity of the materials. High quantities of paraffins and aromatics were formed on MFI, which decreased to medium concentrations on TON, in favor of olefins. On *MRE, almost exclusively olefins were produced, extinguishing other hydrocarbons from the product spectrum. By examination of HTI_{C_3} and C_3/C_2 it can be assumed that formation of products via the aromatic cycle is almost completely suppressed inside the *MRE

pores. Thus, the exceptional high content of more than 90% olefins within the C₃-C₁₁ product fraction is most probably generated via the olefin cycle. Simultaneously, significantly increased *MRE catalyst stability was found compared to previous reports [15,23,24], enabling a cumulative conversion capacity of more than 100 g_{DME} g_{Catalyst}⁻¹. This can be attributed to the minimized formation of deactivating aromatic species inside the catalyst pores.

Furthermore, a strong dependency of DTH product formation and catalyst deactivation on reaction conditions was observed. It became evident, that the effects of altered reaction environment strongly depend on the nature of the zeolite catalyst, in particular on the dimensionality of the pore system. Thus, it was impossible to derive general trends that are valid for different zeolite framework types. Most beneficial conditions for DTH conversion on zeolites *MRE and TON were medium temperature (673 K), low WHSV (1.5 h⁻¹ and 0.3 h⁻¹, respectively) and high DME partial pressure (100 kPa). Under these conditions, the disadvantages of lower temperatures (slow build-up of the autocatalytic HCP and low aromatic dealkylation rate), higher temperatures (formation of strongly chemisorbed aromatics), low $\tau_0/\tau_{0,crit}$ ratio (slow HCP build-up) and low DME concentration (increase of secondary reactions) can be minimized. Such conditions counteract the steric constraints of the narrow one-dimensional 10-ring pore channels enabling a high cumulative conversion capacity and a high C₅₊ yield. For MFI, a lower reaction temperature, comparably high WHSV and low DME partial pressure are favorable for high cumulative conversion capacity and/or C₅₊ yield. As the three-dimensional pore system is accessible for partial substituted methylbenzenes, which facilitate fast HCP build-up and exhibit high reactivity as well as high tolerance for secondary reactions, no inhibition by the corresponding mechanistic effects inside the zeolite channels was observed. This way, a wider range of reaction conditions can be utilized for the material, where coking driven by reactants can be minimized.

The new insights into DME conversion on *MRE demonstrate, that this material was undervalued in the past and offers a highly attractive perspective to new MTH/DTH process routes. The combination of a remarkably high cumulative conversion capacity with the unique product selectivity could become a pathway for the production of synthetic jet fuel, e.g. by recycling of light olefins in the process and dimerization/oligomerization of higher olefins in a subsequent process step. Moreover, a great potential for optimizing the catalytic performance by customized design of the *MRE catalyst is evident. For instance, unfavorable material properties such as the high ratio of Lewis/Brønsted acid sites could be reduced. Additionally, proven concepts for improving zeolite catalysts, such as the introduction of mesopores and the development of hierarchical structures, could be employed.

CRedit authorship contribution statement

Benjamin Niethammer: Methodology, Investigation, Formal analysis, Writing – original draft. **Ulrich Arnold:** Funding acquisition, Conceptualization, Supervision, Investigation, Project administration, Writing – review & editing. **Jörg Sauer:** Supervision, Project administration, Conceptualization, Writing – review & editing.

Declaration of Competing Interest

The authors declare that they have no known competing financial interests or personal relationships that could have appeared to influence the work reported in this paper.

Data availability

Data will be made available on request.

Acknowledgments

The authors thank A. Lautenbach (ICP-OES), Dr. T.N. Otto (Ar-physisorption), N.A. Slaby (Ar-physisorption), Dr. T.A. Zevaco (MAS NMR) and Dr. M.C. Zimmermann (REM micrographs) for supporting this work. Financial support from the Ministerium für Wissenschaft, Forschung und Kunst Baden Württemberg (project “Profilregion Mobilitätssysteme Karlsruhe”, project no. AZ.:32-7544-0/76/6) is gratefully acknowledged.

Appendix A. Supplementary material

Supplementary data associated with this article can be found in the online version at doi:10.1016/j.apcata.2023.119021.

References

- [1] M. Stöcker, Methanol-to-hydrocarbons: catalytic materials and their behavior, *Microporous Mesoporous Mater.* 29 (1999) 3–48, [https://doi.org/10.1016/S1387-1811\(98\)00319-9](https://doi.org/10.1016/S1387-1811(98)00319-9).
- [2] F.J. Keil, Methanol-to-hydrocarbons: process technology, *Microporous Mesoporous Mater.* 29 (1999) 49–66, [https://doi.org/10.1016/S1387-1811\(98\)00320-5](https://doi.org/10.1016/S1387-1811(98)00320-5).
- [3] U. Olsbye, S. Svelle, M. Bjørgen, P. Beato, T.V.W. Janssens, F. Joensen, S. Bordiga, K.P. Lillerud, Conversion of methanol to hydrocarbons: how zeolite cavity and pore size controls product selectivity, *Angew. Chem. Int. Ed.* 51 (2012) 5810–5831, <https://doi.org/10.1002/anie.201103657>.
- [4] Z. Azizi, M. Rezaeimanesh, T. Tohidian, M.R. Rahimpour, Dimethyl ether: a review of technologies and production challenges, *Chem. Eng. Process. Process Intensif.* 82 (2014) 150–172, <https://doi.org/10.1016/j.cep.2014.06.007>.
- [5] S. Polierer, D. Guse, S. Wild, K. Herrera Delgado, T.N. Otto, T.A. Zevaco, M. Kind, J. Sauer, F. Studt, S. Pitter, Enhanced direct dimethyl ether synthesis from CO₂-rich syngas With Cu/ZnO/ZrO₂ catalysts prepared by continuous co-precipitation, *Catalysts* 10 (2020) 816, <https://doi.org/10.3390/catal10080816>.
- [6] N. Delgado Otalvaro, G. Sogne, K. Herrera Delgado, S. Wild, S. Pitter, J. Sauer, Kinetics of the direct DME synthesis from CO₂ rich syngas under variation of the CZA-to- γ -Al₂O₃ ratio of a mixed catalyst bed, *RSC Adv.* 11 (2021) 24556, <https://doi.org/10.1039/D1RA03452A>.
- [7] S. Lee, M. Gogate, C.J. Kulik, Methanol-to-gasoline vs. DME-to-gasoline II. Process comparison and analysis, *Fuel Sci. Technol. Int* 13 (1995) 1039–1057, <https://doi.org/10.1080/08843759508947721>.
- [8] S. Svelle, S. Kolboe, O. Swang, U. Olsbye, Methylation of alkenes and methylbenzenes by dimethyl ether or methanol on acidic zeolites, *J. Phys. Chem. B* 106 (2005) 12874–12878, <https://doi.org/10.1021/jp051125z>.
- [9] P.N. Plessow, A. Smith, S. Tischer, F. Studt, Identification of the reaction sequence of the initiation mechanism using ab initio-based kinetics, *J. Am. Chem. Soc.* 141 (2019) 5908–5915, <https://doi.org/10.1021/jacs.9b00585>.
- [10] P. Pérez-Urriarte, A. Ateka, A.T. Aguayo, G.G. Gayubo, J. Bilbao, Kinetic model for the reaction of DME to olefins over a HZSM-5 zeolite catalyst, *Chem. Eng. J.* 302 (2016) 801–810, <https://doi.org/10.1016/j.ces.2016.05.096>.
- [11] J.S. Martínez-Espin, M. Mortén, T.V.W. Janssens, S. Svelle, P. Beato, U. Olsbye, New insights into catalyst deactivation and product distribution of zeolites in the methanol-to-hydrocarbons (MTH) reaction with methanol and dimethyl ether feeds, *Catal. Sci. Technol.* 7 (2017) 2700, <https://doi.org/10.1039/C7CY00129K>.
- [12] M. Bjørgen, S. Svelle, F. Joensen, J. Nerlov, S. Kolboe, F. Bonino, L. Palumbo, S. Boediga, U. Olsbye, Conversion of methanol to hydrocarbons over zeolite H-ZSM-5: on the origin of the olefinic species, *J. Catal.* 249 (2007) 195–207, <https://doi.org/10.1016/j.jcat.2007.04.006>.
- [13] I.M. Dahl, S. Kolboe, On the reaction mechanism for hydrocarbon formation from methanol over SAPO-34: 1. isotopic labeling studies of the co-reaction of ethene and methanol, *J. Catal.* 149 (1994) 458–464, <https://doi.org/10.1006/jcat.1994.1312>.
- [14] I.M. Dahl, S. Kolboe, On the reaction mechanism for hydrocarbon formation from methanol over SAPO-34: 2. isotopic labeling studies of the co-reaction of propene and methanol, *J. Catal.* 161 (1996) 304–309, <https://doi.org/10.1006/jcat.1996.0188>.
- [15] S. Teketel, W. Skistad, S. Benard, U. Olsbye, K.P. Lillerud, P. Beato, S. Svelle, Shape selectivity in the conversion of methanol to hydrocarbons: the catalytic performance of one-dimensional 10-ring zeolites: ZSM-22, ZSM-23, ZSM-48, and EU-1, *ACS Catal.* 2 (2012) 26–37, <https://doi.org/10.1021/cs200517u>.
- [16] S. Teketel, U. Olsbye, K.P. Lillerud, P. Beato, S. Svelle, Selectivity control through fundamental mechanistic insight in the conversion of methanol to hydrocarbons over zeolites, *Microporous Mesoporous Mater.* 136 (2010) 33–41, <https://doi.org/10.1016/j.micromeso.2010.07.013>.
- [17] S. Teketel, S. Svelle, K.P. Lillerud, U. Olsbye, Shape selective conversion of methanol to hydrocarbons over 10-ring unidirectional-channel acidic H-ZSM-22, *ChemCatChem* 1 (2009) 78–81, <https://doi.org/10.1002/cctc.200900057>.
- [18] P. del Campo, U. Olsbye, K.P. Lillerud, S. Svelle, P. Beato, Impact of post-synthetic treatments on unidirectional H-ZSM-22 zeolite catalyst: towards improved clean MTG catalytic process, *Catal. Today* 299 (2018) 135–145, <https://doi.org/10.1016/j.cattod.2017.05.011>.

- [19] J. Wang, S. Xu, J. Li, Y. Zhi, M. Zhang, Y. He, Y. Wei, X. Guo, Z. Liu, An approach to prepare nanosized HZSM-22 with enhanced lifetime in the methanol to hydrocarbon (MTH) reaction, *RSC Adv.* (2015) 88928, <https://doi.org/10.1039/C5RA18438J>.
- [20] M. Dyballa, U. Obenaus, M. Rosenberger, A. Fischer, H. Jakob, E. Klemm, M. Hunger, Post-synthetic improvement of H-ZSM-22 zeolites for the methanol-to-olefin conversion, *Microporous Mesoporous Mater.* 233 (2016) 26–30, <https://doi.org/10.1016/j.micromeso.2016.06.044>.
- [21] R.F. Lobo, H. van Koningsveld, New description of the disorder in zeolite ZSM-48, *J. Am. Chem. Soc.* 124 (2002) 13222–13230, <https://doi.org/10.1021/ja020569v>.
- [22] G.F. Froment, W.J.H. Dehertog, A.J. Marchi, Zeolite catalysis in the conversion of methanol into olefins, *Catalysis* 9 (1992) 1–64, <https://doi.org/10.1039/9781847553218-00001>.
- [23] S. Teketel, L.F. Lundegaard, W. Skistad, S.M. Chavan, U. Olsbye, K.P. Lillerud, P. Beato, S. Svelle, Morphology-induced shape selectivity in zeolite catalysis, *J. Catal.* 327 (2015) 22–32, <https://doi.org/10.1016/j.jcat.2015.03.013>.
- [24] J. Zhang, Z. Huang, L. Xu, X. Zhang, X. Zhang, Y. Yuan, L. Xu, Verifying the olefin formation mechanism of the methanol-to-hydrocarbons reaction over H-ZSM-48, *Catal. Sci. Technol.* 9 (2019) 2132–2143, <https://doi.org/10.1039/C8CY02621A>.
- [25] D.H. Olson, G.T. Kokotailo, S.L. Lawton, W.M. Meier, Crystal structure and structure-related properties of ZSM-5, *J. Phys. Chem.* 85 (1981) 2238–2243, <https://doi.org/10.1021/j150615a020>.
- [26] J.L. Schlenker, W.J. Rohrbaugh, P. Chu, E.W. Valyocsik, G.T. Kokotailo, The framework topology of ZSM-48: a high silica zeolite, *Zeolites* 5 (1985) 355–358, [https://doi.org/10.1016/0144-2449\(85\)90124-1](https://doi.org/10.1016/0144-2449(85)90124-1).
- [27] G.T. Kokotailo, J.L. Schlenker, F.G. Dwyer, E.W. Valyocsik, The framework topology of ZSM-22: A high silica zeolite, *Zeolites* 5 (1985) 349–351, [https://doi.org/10.1016/0144-2449\(85\)90122-8](https://doi.org/10.1016/0144-2449(85)90122-8).
- [28] International Organization for Standardization, Pore Size Distribution and Porosity of Solid Materials by Mercury Porosimetry and Gas Adsorption – Part 3: Analysis of Micropores by Gas Adsorption, ISO 15091-3:2007, Switzerland, 2007.
- [29] J. Rouquerol, P. Llewellyn, F. Rouquerol, Is the BET equation applicable to microporous adsorbents? *Stud. Surf. Sci. Catal.* 160 (2007) 49–56, [https://doi.org/10.1016/S0167-2991\(07\)80008-5](https://doi.org/10.1016/S0167-2991(07)80008-5).
- [30] International Organization for Standardization, Determination of the Specific Surface Area of Solids by Gas Adsorption – BET Method, ISO 9277:2010, Switzerland, 2010.
- [31] U. Bentrup, A. Martin, B. Lücke, Infrared characterization of the surface intermediates in the oxidation of toluene on vanadyl pyrophosphate catalysts, *Top. Catal.* 11 (2000) 139–145, <https://doi.org/10.1023/A:1027234116582>.
- [32] C.A. Emeis, Determination of integrated molar extinction coefficients for infrared absorption bands of pyridine adsorbed on solid acid catalysts, *J. Catal.* 141 (1993) 347–354, <https://doi.org/10.1006/jcat.1993.1145>.
- [33] H. Schulz, “Coking” of zeolites during methanol conversion: Basic reactions of the MTO-, MTP- and MTG processes, *Catal. Today* 154 (2010) 183–194, <https://doi.org/10.1016/j.cattod.2010.05.012>.
- [34] International Organization for Standardization, Liquid Petroleum Products – Determination of Hydrocarbon Types and Oxygenates in Automotive-motor Gasoline and in Ethanol (E85) Automotive Fuel – Multidimensional Gas Chromatography Method, ISO 22854:2021, Switzerland, 2021.
- [35] M.C. Zimmermann, T.N. Otto, S. Wodarz, T.A. Zevaco, S. Pitter, Mesoporous H-ZSM-5 for the conversion of dimethyl ether to hydrocarbons, *Chem. Ing. Tech.* 91 (2019) 1302–1313, <https://doi.org/10.1002/cite.201800217>.
- [36] M. Thommes, K. Kaneko, A.V. Neimark, J.P. Olivier, F. Rodriguez-Reinos, J. Rouquerol, K.S.W. Sing, Physisorption of gases, with special reference to the evaluation of surface area and pore size distribution (IUPAC technical report), *Pure Appl. Chem.* 87 (2015) 1051–1069, <https://doi.org/10.1515/pac-2014-1117>.
- [37] P.A. Jacobs, J.A. Martens, Chapter I: synthesis of ZSM-5 zeolites in the presence of tetrapropylammonium ions, *Stud. Surf. Sci. Catal.* 33 (1987) 47–111, [https://doi.org/10.1016/S0167-2991\(09\)60467-5](https://doi.org/10.1016/S0167-2991(09)60467-5).
- [38] X. Liu, X. Wang, Y. Wang, Y. Gong, T. Dou, Synthesis and characterization of hierarchical ZSM-48 zeolite, *Adv. Mater. Res.* 503–504 (2012) 756–759, <https://doi.org/10.4028/www.scientific.net/AMR.503-504.756>.
- [39] P. del Campo, W.A. Slawinski, R. Henry, M.W. Erichsen, S. Svelle, P. Beato, D. Wragg, U. Olsbye, Time- and space-resolved high energy operando X-ray diffraction for monitoring the methanol to hydrocarbons reaction over H-ZSM-22 zeolite catalyst in different conditions, *Surf. Sci.* 648 (2016) 141–149, <https://doi.org/10.1016/j.susc.2015.10.049>.
- [40] R.M. Highcock, G.W. Smith, D. Wood, Structure of the new zeolite theta-1 determined from X-ray powder data, *Acta Crystallogr. C* 41 (1985) 1391–1394, <https://doi.org/10.1107/S0108270185007892>.
- [41] C.A. Fyfe, Y. Feng, H. Grondey, Evaluation of chemical shift-structure correlations from a combination of X-ray diffraction and 2D MAS NMR data for highly siliceous zeolite frameworks, *Microporous Mater.* 1 (1993) 393–400, [https://doi.org/10.1016/0927-6513\(93\)80034-R](https://doi.org/10.1016/0927-6513(93)80034-R).
- [42] C.A. Fyfe, H. Strobl, G.T. Kokotailo, G.J. Kennedy, G.E. Barlow, Ultra-high-resolution ^{29}Si solid-state MAS NMR investigation of sorbate and temperature-induced changes in the lattice structure of zeolite ZSM-5, *J. Am. Chem. Soc.* 110 (1988) 3373–3380, <https://doi.org/10.1021/ja00219a005>.
- [43] C.A. Fyfe, H. Grondey, Y. Feng, G.T. Kokotailo, Natural-abundance two-dimensional ^{29}Si MAS NMR investigation of the three-dimensional bonding connectivities in the zeolite catalyst ZSM-5, *J. Am. Chem. Soc.* 112 (1990) 8812–8820, <https://doi.org/10.1021/ja00180a024>.
- [44] D.G. Hay, H. Jaeger, Orthorhombic-monoclinic phase changes in ZSM-5 zeolite/silicate, *J. Chem. Soc. Chem. Commun.* (1984) 1433, <https://doi.org/10.1039/C39840001433>.
- [45] P. Sarv, C. Fernandez, J.P. Amoureux, K. Keskinen, Distribution of tetrahedral aluminium sites in ZSM-5 type zeolites: an ^{27}Al (multi-quantum) magic angle spinning NMR study, *J. Phys. Chem.* 100 (1996) 19223–19226, <https://doi.org/10.1021/jp962519g>.
- [46] T. Blasco, A. Corma, J. Martínez-Triguero, Hydrothermal stabilization of ZSM-5 catalytic-cracking additives by phosphorus addition, *J. Catal.* 237 (2006) 267–277, <https://doi.org/10.1016/j.jcat.2005.11.011>.
- [47] C.A. Fyfe, G.T. Kokotailo, H. Strobl, C.S. Pasztor, G. Barlow, S. Bradley, Combined use of nuclear magnetic resonance, electron microscopy, and diffraction techniques as a probe of the uniqueness of zeolite structures: zeolites KZ-2, Theta-1, ZSM-22, and NU-10, *Zeolites* 9 (1989) 531–534, [https://doi.org/10.1016/0144-2449\(89\)90050-X](https://doi.org/10.1016/0144-2449(89)90050-X).
- [48] C.A. Fyfe, Y. Feng, H. Gies, H. Grondey, G.T. Kokotailo, Natural-abundance two-dimensional solid-state ^{29}Si NMR investigations of three-dimensional lattice connectivities in zeolite structures, *J. Am. Chem. Soc.* 112 (1990) 3264–3270, <https://doi.org/10.1021/ja00165a002>.
- [49] M. Derewinski, P. Sarv, A. Mifsud, Thermal stability and siting of aluminum in isostructural ZSM-22 and Theta-1 zeolites, *Catal. Today* 114 (2006) 197–204, <https://doi.org/10.1016/j.cattod.2006.01.008>.
- [50] M. Zhang, L. Wang, Y. Chen, Q. Zhang, C. Liang, Creating mesopores in ZSM-48 by alkali treatment: enhanced catalyst for hydroisomerization of hexadecane, *J. Energy Chem.* 25 (2016) 539–544, <https://doi.org/10.1016/j.jechem.2016.01.014>.
- [51] J. Meng, C. Li, X. Chen, C. Song, C. Liang, Seed-assisted synthesis of ZSM-48 zeolite with low $\text{SiO}_2/\text{Al}_2\text{O}_3$ ratio for *n*-hexadecane hydroisomerization, *Microporous Mesoporous Mater.* 309 (2020), 110565, <https://doi.org/10.1016/j.micromeso.2020.110565>.
- [52] M. Guisnet, P. Magnoux, D. Martin, Roles of acidity and pore structure in the deactivation of zeolites by carbonaceous deposits, *Stud. Surf. Sci. Catal.* 111 (1997) 1–19, [https://doi.org/10.1016/S0167-2991\(97\)80138-3](https://doi.org/10.1016/S0167-2991(97)80138-3).
- [53] M. Guisnet, L. Costa, F. Ramôa Ribeiro, Prevention of zeolite deactivation by coking, *J. Mol. Catal. A Chem.* 305 (2009) 69–83, <https://doi.org/10.1016/j.molcata.2008.11.012>.
- [54] D. Mores, J. Kornatowski, U. Olsbye, B.M. Weckhuysen, Coke formation during the methanol-to-olefin conversion: in situ microspectroscopy on individual H-ZSM-5 crystals with different Brønsted acidity, *Chem. Eur. J.* 17 (2011) 2874–2884, <https://doi.org/10.1002/chem.201002624>.
- [55] B.A. Sexton, A.E. Hughes, D.M. Bibby, An XPS study of coke distribution on ZSM-5, *J. Catal.* 109 (1988) 126–131, [https://doi.org/10.1016/0021-9517\(88\)90190-X](https://doi.org/10.1016/0021-9517(88)90190-X).
- [56] H. Schulz, M. Wei, Pools and constraints in methanol conversion to olefins and fuels on zeolite HZSM5, *Top. Catal.* 57 (2014) 683–692, <https://doi.org/10.1007/s11244-013-0225-9>.
- [57] D.A. Simonetti, J.H. Ahn, E. Iglesia, Mechanistic details of acid-catalyzed reactions and their role in the selective synthesis of triptane and isobutene from dimethyl ether, *J. Catal.* 277 (2011) 173–195, <https://doi.org/10.1016/j.jcat.2010.11.004>.
- [58] D.A. Simonetti, R.T. Carr, E. Iglesia, Acid strength and solvation effects on methylation, hydride transfer, and isomerization rates during catalytic homologation of C_1 species, *J. Catal.* 285 (2012) 19–30, <https://doi.org/10.1016/j.jcat.2011.09.007>.
- [59] Ø. Mikkelsen, S. Kolboe, The conversion of methanol to hydrocarbons over zeolite H-beta, *Microporous Mesoporous Mater.* 29 (1999) 173–184, [https://doi.org/10.1016/S1387-1811\(98\)00329-1](https://doi.org/10.1016/S1387-1811(98)00329-1).
- [60] S. Svelle, F. Joensen, J. Nerlov, U. Olsbye, K.P. Lillerud, S. Kolboe, M. Bjørgen, Conversion of methanol into hydrocarbons over zeolite H-ZSM-5: ethene formation is mechanistically separated from the formation of higher alkenes, *J. Am. Chem. Soc.* 128 (2006) 14770–14771, <https://doi.org/10.1021/ja065810a>.
- [61] S. Svelle, P.O. Rønning, S. Kolboe, Kinetic studies of zeolite-catalyzed methylation reactions 1. Coreaction of ^{12}C ethane and ^{13}C methanol, *J. Catal.* 224 (2004) 115–123, <https://doi.org/10.1016/j.jcat.2004.02.022>.
- [62] S. Svelle, P.O. Rønning, U. Olsbye, S. Kolboe, Kinetic studies of zeolite-catalyzed methylation reactions. Part 2. Co-reaction of ^{12}C propene or ^{12}C *n*-butene and ^{13}C methanol, *J. Catal.* 234 (2005) 385–400, <https://doi.org/10.1016/j.jcat.2005.06.028>.
- [63] S. Svelle, U. Olsbye, F. Joensen, M. Bjørgen, Conversion of methanol to alkenes over medium- and large-pore acidic zeolites: steric manipulation of the reaction intermediates governs the ethene/propene product selectivity, *J. Phys. Chem. C* 111 (2007) 17981–17984, <https://doi.org/10.1021/jp077331j>.
- [64] M. Bjørgen, F. Joensen, K.P. Lillerud, U. Olsbye, S. Svelle, The mechanisms of ethene and propene formation from methanol over high silica H-ZSM-5 and H-beta, *Catal. Today* 142 (2009) 90–97, <https://doi.org/10.1016/j.cattod.2009.01.015>.
- [65] G.J. Hutchings, F. Gottschalk, R. Hunter, Comments on “kinetic model for methanol conversion to olefins” with respect to methane formation at low conversion, *Ind. Eng. Chem. Res.* 26 (1987) 635–637, <https://doi.org/10.1021/ie00063a041>.
- [66] X. Sun, S. Mueller, Y. Liu, H. Shi, G.L. Haller, M. Sanchez-Sanchez, A.C. van Veen, J.A. Lercher, On reaction pathways in the conversion of methanol to hydrocarbons on HZSM-5, *J. Catal.* 317 (2014) 185–197, <https://doi.org/10.1016/j.jcat.2014.06.017>.
- [67] S. Müller, Y. Liu, M. Vishnuvarthan, X. Sun, A.C. van Veen, G.L. Haller, M. Sanchez-Sanchez, J.A. Lercher, Coke formation and deactivation pathways on H-ZSM-5 in the conversion of methanol to olefins, *J. Catal.* 325 (2015) 48–59, <https://doi.org/10.1016/j.jcat.2015.02.013>.
- [68] M. Bjørgen, U. Olsbye, S. Kolboe, Coke precursor formation and zeolite deactivation: mechanistic insights from hexamethylbenzene conversion, *J. Catal.* 215 (2003) 30–44, [https://doi.org/10.1016/S0021-9517\(02\)00050-7](https://doi.org/10.1016/S0021-9517(02)00050-7).

- [69] M. Bjørgen, U. Olsbye, S. Svelle, S. Kolboe, Conversion of methanol to hydrocarbons: the reactions of the heptamethylbenzenium cation over zeolite H-beta, *Catal. Lett.* 93 (2004) 37–40, <https://doi.org/10.1023/B:CATL.0000016945.28495.f0>.
- [70] J.F. Haw, D.M. Marcus, Well defined (supra)molecular structures in zeolite methanol-to-olefin catalysis, *Top. Catal.* 34 (2005) 41–48, <https://doi.org/10.1007/s11244-005-3798-0>.
- [71] M. Bjørgen, U. Olsbye, D. Petersen, S. Kolboe, The methanol-to-hydrocarbons reaction: insight into the reaction mechanism from [¹²C]benzene and [¹³C] methanol coreactions over zeolite H-beta, *J. Catal.* 221 (2004) 1–10, [https://doi.org/10.1016/S0021-9517\(03\)00284-7](https://doi.org/10.1016/S0021-9517(03)00284-7).
- [72] B.E. Langner, Reactions of methanol on zeolites with different pore structures, *Appl. Catal.* 2 (1982) 289–302, [https://doi.org/10.1016/0166-9834\(82\)80075-4](https://doi.org/10.1016/0166-9834(82)80075-4).
- [73] S. Mueller, Y. Liu, F.M. Kirchberger, M. Tonigold, M. Sanchez-Sanchez, J. A. Lercher, Hydrogen transfer pathways during zeolite catalyzed methanol to hydrocarbons, *J. Am. Chem. Soc.* 138 (2016) 15994–16003, <https://doi.org/10.1021/jacs.6b09605>.
- [74] Y. Liu, S. Müller, D. Berger, J. Jelic, K. Reuter, M. Tonigold, M. Sanchez-Sanchez, J. A. Lercher, *Angew. Chem. Int. Ed.* 55 (2016) 5723–5726, <https://doi.org/10.1002/ange.201511678>.
- [75] W. Dai, C. Wang, M. Dybala, G. Wu, N. Guan, L. Li, Z. Xie, M. Hunger, Understanding the early stages of the methanol-to-olefin conversion on H-SAPO-34, *ACS Catal.* 5 (2015) 317–326, <https://doi.org/10.1021/cs5015749>.
- [76] T.V.W. Janssens, S. Svelle, U. Olsbye, Kinetic modeling of deactivation profiles in the methanol-to-hydrocarbons (MTH) reaction: a combined autocatalytic-hydrocarbon pool approach, *J. Catal.* 308 (2013) 122–130, <https://doi.org/10.1016/j.jcat.2013.05.035>.
- [77] D.S. Wragg, M.G. O'Brien, F.L. Bleken, M. Di Michiel, U. Olsbye, H. Fjellvåg, Watching the methanol-to-olefin process with time- and space-resolved high-energy operando X-ray diffraction, *Angew. Chem.* 124 (2012) 8080–8083, <https://doi.org/10.1002/ange.201203462>.
- [78] F.L. Bleken, T.V.W. Janssens, S. Svelle, U. Olsbye, Product yield in methanol conversion over ZSM-5 is predominantly independent of coke content, *Microporous Mesoporous Mater.* 164 (2012) 190–198, <https://doi.org/10.1016/j.micromeso.2012.06.020>.
- [79] D. Rojo-Gama, S. Etemadi, E. Kirby, K.P. Lillerud, P. Beato, S. Svelle, U. Olsbye, Time- and space-resolved study of the methanol to hydrocarbons (MTH) reaction – influence of zeolite topology on axial deactivation patterns, *Faraday Discuss.* 197 (2017) 421, <https://doi.org/10.1039/C6FD00187D>.
- [80] W.J.H. Dehertog, G.F. Froment, Production of light alkenes from methanol on ZSM-5 catalysts, *Appl. Catal.* 71 (1991) 153–165, [https://doi.org/10.1016/0166-9834\(91\)85012-K](https://doi.org/10.1016/0166-9834(91)85012-K).
- [81] C.D. Chang, W.H. Lang, R.L. Smith, The conversion of methanol and other O-compounds to hydrocarbons over zeolite catalysts: II. Pressure effects, *J. Catal.* 56 (1979) 169–173, [https://doi.org/10.1016/0021-9517\(79\)90103-9](https://doi.org/10.1016/0021-9517(79)90103-9).